ACS APPLIED MATERIALS & INTERFACES

Research Article

www.acsami.org

Synthesis of Amorphous Platinum Nanofibers Directly on an ITO Substrate and Its Heterogeneous Catalytic Hydrogenation Characterization

Aamna Balouch,[†,‡] Akrajas Ali Umar,*[,†] Elvy Rahmi Mawarnis,[†] Siti Khatijah Md Saad,[†] Muhamad Mat Salleh,[†] Mohd Yusri Abd Rahman,[†] I. V. Kityk,[§] and Munetaka Oyama[∥]

[†]Institute of Microengineering and Nanoelectronics, Universiti Kebangsaan Malaysia, 43600 UKM Bangi, Selangor, Malaysia

[‡]National Center of Excellence in Analytical Chemistry, University of Sindh, Jamshoro, Pakistan

[§]Electrical Engineering Department, Institute of Electronic System, Technical University of Czestochowa, Czestochowa, Poland

[∥]Department of Material Chemistry, Graduate School of Engineering, Kyoto University, Nishikyo-ku, Kyoto, 615-8520, Japan

Supporting Information

ABSTRACT: This paper reports a facile, solution-phase approach to synthesizing a one-dimensional amorphous face-centered-cubic (fcc) platinum (a-Pt) nanostructure (nanofibers) directly on an indium−tin oxide (ITO) substrate. The electron microscopy analysis result shows that the a-Pt nanofiber has a diameter and length of approximately 50 nm and 1 μm, respectively, and is grown in high density on the entire surface of the ITO substrate. The X-ray photoelectron spectroscopy analysis result further reveals that the a-Pt nanofibers feature metallic properties with highly reactive surface chemistry, promising novel performance in electrochemistry, catalysis, and sensors. A synergetic interplay between the formic acid reducing agent and the hexamethylenetetramine surfactant in the reduction of Pt ions is assumed as the driving force for the formation of the amorphous phase in the Pt nanostructure. The catalytic properties of a-Pt were examined in the acetone hydrogenation reaction under microwave irradiation. a-Pt shows excellent heterogeneous catalytic properties for converting acetone to isopropyl alcohol with turnover number and frequency as high as 400 and 140 min^{-1}, respectively. The preparation and formation mechanism of the a-Pt nanofibers will be discussed in detail in this paper.

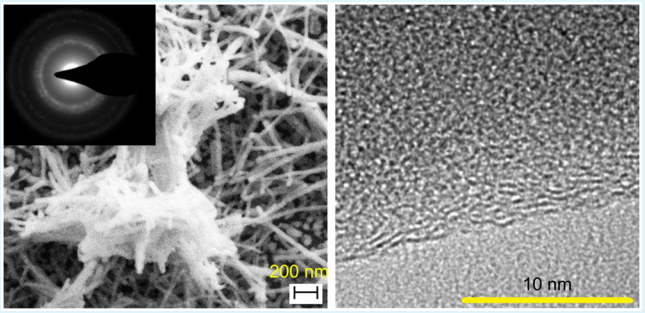

KEYWORDS: *amorphous metal, platinum, nanofibers, chemical synthesis, catalysis*

1. INTRODUCTION

Platinum (Pt) nanocrystals[1−3] have recently received significant attention for use in a broad range of applications ranging from catalysis[4−9] to dye-sensitized solar cells,[10,11] electrocatalysis,[12] and sensing[13] because of their peculiar electrical and catalytic properties. The performance of the Pt nanocrystals in application is strongly determined by the morphology and nature of the atomic arrangement, the orientation at the surface, and the bulk of the nanocrystal. The synthesis of Pt nanostructures with different morphologies[14] as well as new crystallographic structures or allotropes, such as amorphous, promises novel properties, expanding their performance in applications. Amorphous Pt (a-Pt) nanostructure with a disordered atomic arrangement either on the surface or in the bulk structure is expected to produce unique surface chemistry and electrical properties that are presumably superior to its crystalline structure because of the peculiar interatomic interplay. For example, the amorphous nanostructure of Pt may have highly reactive surface properties resulting from the enhancement of the physicochemical properties of the individual Pt atoms due to the decreasing of the interatomic interaction, the effect of the disordered atomic arrangement, and less dense bulk and surface atoms. The a-Pt nanostructure may also have unusual strength because of an improvement of the shear resistance from the high flexibility of the disordered atomic arrangement in the nanostructure.[15,16] With less dense atoms in the structure, a-Pt is expected to show unusual electrical and optical properties because of the high degree of anisotropy of electron-wave overlap.[17] Therefore, there should be a significant effort to synthesize a-Pt nanostructures.

Amorphism in the Pt nanocrystal has not yet been observed. The inherently strong metallic bonding properties that easily arrange Pt nanocrystals into highly symmetric face-centered-cubic (fcc) crystals make allotropism almost improbable in the pure metal system.[18] Although amorphous metals mainly synthetically exist in alloys, such as AuSi,[19] FeNiB,[20] CuZrAl,[21]

Received: February 3, 2015
Accepted: March 25, 2015
Published: March 25, 2015

DOI: 10.1021/acsami.5b01012
ACS Appl. Mater. Interfaces 2015, 7, 7776−7785

CeAlCu,[22] and MgCuY,[23] a limited number of pure metals can also be prepared in the amorphous form, such as iron (Fe),[24] tantalum (Ta),[25] and nickel (Ni).[26] Similar to the amorphous metal alloys, pure metals are normally prepared using a rapid cooling process or thermal quenching.[25] Although showing efficient amorphous structure formation, the procedure is complicated, involving precise control over the thermal-quenching process to achieve an in-equilibrium solidification process. Because the process is harsh, involving an abrupt thermal quenching (up to 10^{10} K s^{-1}),[25] the yield is also predicted to be low and uncontrollable because the process strongly depends on the nature of the quenching and the volume of the reaction. A sonochemical approach has been demonstrated for a "mild" amorphous metal preparation.[24] Unfortunately, because acoustic cavitation induction for realization of the glassy state in Fe is also a position-dependent process, the yield is also low and uncontrollable. Recently, a phase-transfer process was proposed for an effective and mild process for amorphous palladium (Pd) synthesis.[27] Nevertheless, although facile formation of amorphous Pd was observed, the process required careful control over the nanostructure resolidification during the phase-transfer process, involving the use of surfactant molecules with special chemistry, which is predicted to be unique and limited to a particular metal system. In this study, we develop a straightforward strategy to synthesize a-Pt via a low-temperature aqueous chemical reaction process. By following a simple and mild aqueous solution-phase reaction containing a formic acid reductant and a hexamethylenetetramine (HMT) surfactant and by controlling the reaction conditions, such as the precursor and surfactant concentrations and growth temperature, we achieved the formation of large-scale a-Pt nanofibers directly on the substrate surface. We believe that a unique synergetic function between the formic acid reducing agent and the HMT surfactant during the reduction of Pt ions and the crystallization in aqueous reaction is the driving force for the formation of the amorphous structure in this pure metal system. The presence of the amorphous structure provides evidence of the capability to prepare highly symmetry fcc Pt as a structure that is far beyond its natural fcc symmetry. More novel properties are expected from this new structure of Pt. The heterogeneous catalytic property of the a-Pt nanofibers was examined in the hydrogenation reaction of acetone to isopropyl alcohol under microwave irradiation. The heterogeneous catalytic reaction efficiency is considerably high, with a turnover frequency (TOF) and a turnover number (TON) as high as 140 min^{-1} and 400, respectively. The a-Pt nanofibers catalyst has the potential for use as a green approach for the production of isopropyl alcohol.

2. EXPERIMENTAL SECTION

2.1. a-Pt Nanofiber Preparation. a-Pt nanofiber growth on an indium−tin oxide (ITO) surface was promoted using a liquid-phase deposition method.[8,28,29] To achieve the optimum growth of a-Pt nanofibers on the ITO surface, reduction of the Pt complex was performed in highly reducing conditions utilizing a formic acid reductant. In a typical experimental procedure, a clean ITO substrate (sheet resistance of 7−11 Ω $\square^{-1}$ purchased from Kaivo, China), which was washed by consecutive ultrasonication in acetone and ethanol for 30 min, was immersed in 15 mL of an aqueous growth solution containing 10 mM hexamethylenetetramine (HMT; Sigma), 1 mM potassium hexachloroplatinate (K_2PtCl_6; Fluka), and 1.0 M formic acid (Fluka). The solution was continuously stirred during the growth process. The growth process was performed at 40 °C for 5 h. After completion of the growth process, the sample was removed from the growth solution, rinsed with a copious amount of deionized water, and dried with a flow of nitrogen gas.

All chemicals were used as received without any further purification process. Pure water was used throughout the reaction and was obtained from a Milli-Q water purification system.

2.2. Nanostructure Characterization. The morphology of the a-Pt nanofibers was examined using field-emission scanning electron microscopy (FESEM; Hitachi S-4800) operating at an accelerating voltage of 5 kV. Its bulk structure and crystallinity were examined using scanning transmission electron microscopy (STEM; FEI Tecnai G2 F20) with an X-twin objective lens operating at an accelerating voltage and vacuum level of 200 kV and 10^{-6} Pa, respectively, which result in a STEM HAADF resolution as high as 0.16 nm. The instrument was equipped for energy-dispersive X-ray (EDX) analysis with an X-max 80T detector (Oxford Instruments) for elemental mapping of the a-Pt nanofibers. The crystal structure and phase of the samples were characterized by X-ray diffraction using a Bruker D8 Advance system with Cu Kα irradiation (λ = 1.541 Å) at a scan rate of 10° min^{-1}. The chemical state of the sample was characterized by X-ray photoelectron spectroscopy (XPS) using a Kratos XSAM-HS apparatus with Al Kα radiation. In the analysis, a Shirley-type background was used for the curve-fitting process with a Gaussian−Lorentzian (GL) mixed function background (70% and 30% for the Gaussian and Lorentzian components, respectively) as the line shaping. The calibration curve for the core-level spectra was referenced to C 1s with a binding energy of 285 eV. Fourier transform infrared (FTIR) spectroscopy was also carried out on the sample to determine its molecular and lattice vibration by using a PerkinElmer Spectrum 400 FTIR/FT-NIR. The FTIR machine was equipped with polystyrene as a baseline along with a deuterated triglycine sulfate detector and an attenuated total reflectance (ATR-50) analysis method. The scan speed used during characterization of the samples was 750 nm min^{-1} with the interval of as low as 4 nm.

The Brunauer−Emmett−Teller (BET) surface areas of the a-Pt nanofibers were determined by a nitrogen adsorption−desorption analysis at −195.816 °C using a Micromeritic 2020 apparatus. The samples were degassed at 300 °C for 480 min prior to nitrogen adsorption measurements. The weight of the sample after degassing was recorded. The total weight of the sample used in this study was 1 g (a-Pt nanofibers + substrate).

2.3. Heterogeneous Catalytic Characterization. The heterogeneous catalytic properties of the Pt nanofibers were evaluated by the hydrogenation of acetone to isopropyl alcohol under microwave irradiation. In a typical procedure, a glass vial containing 10.0 mL of an aqueous solution of 0.1 mol L^{-1} acetone was placed in a Teflon-sealed vial and was irradiated with microwaves (Panasonic home appliances microwave oven model NN-GDS577M) in the absence and presence of the a-Pt-nanofiber-attached ITO substrate. The microwave power was as low as 110 W. The kinetic hydrogenation of acetone was evaluated by recording the optical absorption spectrum of the solution every 10 s. For this purpose, a portion of the solution (approximately 4 mL) was removed and transferred into a quartz cuvette. The optical absorption measurement was performed using a PerkinElmer Lambda 900 UV−visible spectrophotometer.

The temperature of the reaction was monitored using a K-type thermocouple (FLUKE 50D). The typical temperature during the reaction inside the microwave chamber was approximately 35 °C. It can be assumed that the contribution of the temperature to the hydrogenation of acetone to isopropyl alcohol in the present conditions was minimal.

To verify the hydrogenation of acetone producing isopropyl alcohol, a high-performance liquid chromatography (HPLC) analysis was performed on the reaction solution using an Agilent 1200 Series Rapid Resolution HPLC system. The apparatus uses a refractive index detector with autosampling via an HPLC pump operated under isocratic elution conditions using a Phenomenex RoA 300 × 7.8 mm column. A 0.005 N H_2SO_4 solution with a 0.6 mL min^{-1} flow rate was used as the mobile phase. The column temperature was kept at 60 °C during the operation.

DOI: 10.1021/acsami.5b01012
ACS Appl. Mater. Interfaces 2015, 7, 7776−7785

To evaluate the efficiency of our system with respect to the amount of catalyst and to compare it with the recently reported results, we calculate the mass of the a-Pt nanofibers on the ITO substrate. A gravimetric method[28,30] was used for this purpose. Briefly, 20 pieces of clean ITO slides (dimensions of 1 × 1.5 cm) were preweighed prior to deposition of the a-Pt nanofibers. To obtain the mass of the a-Pt nanofibers on the ITO surface, the a-Pt-nanofiber-attached ITO surfaces were then reweighed. The difference in the weight of the ITO substrate before and after the attachment of a-Pt nanofibers was considered as the mass of the Pt nanofibers on the ITO surface. The weight of a-Pt nanofibers on a single ITO slide was approximately 30 μg.

Prior to the heterogeneous catalytic hydrogenation of acetone, the concentration of acetone was calculated by plotting the standard calibration graph of acetone, namely, the absorbance at the main absorption band (200−300 nm) of acetone versus its concentration. Figure S1 in the Supporting Information (SI) shows a typical standard calibration graph for acetone obtained in this study. From the plot, a coefficient of regression (R^2) value as high as 0.99 was obtained, reflecting the high accuracy and the sensitivity of the method. The concentration of the acetone was then calculated using the relationship of $y = mx + c$, where y, m, x, and c are the absorbance, slope, concentration, and intercept values, respectively.

3. RESULTS AND DISCUSSION

3.1. a-Pt Nanofiber Characterization. In contrast to the normal characteristics of crystalline Pt nanostructures with a metallic-black color, the a-Pt nanofiber thin films on an ITO substrate exhibit a foggy white color that is formed following short-term immersion in a solution containing a mixed aqueous solution of 1 mM K_2PtCl_6, 10 mM HMT, and 1.0 M formic acid. The initial color of the solution was pale-yellow. With increasing time and under mild and continuous stirring at 400 rpm, the color of the solution gradually changed to colorless and finally turned to a foggy white at a reaction time of approximately 5 h. At this stage, a uniform white film was also formed on the ITO surface.

We conducted FESEM analysis to evaluate the morphology of the nanostructure that was formed on the substrate surface. The result is shown in Figure 1A,B. As parts A and B of Figure 1show, the nanostructures are one-dimensional with diameters and lengths in the ranges of 40−50 and 200−1000 nm, respectively. The yield is approximately 70%, effectively covering the entire surface of the ITO substrate. We call the nanostructure "nanofibers" for simplicity. In addition to the nanofibers, spherical and irregular-shaped nanostructures are formed, occupying the bottom of the ITO surface. Their yield is as low as 30%. In view of their diameter in the range of 20−30 nm, we assume that the nanofibers could be projected from these nanostructures.

After the nanofibers were peeled off of the substrate surface via an ultrasonication process and then transferred onto a carbon-film-coated copper grid, the detailed bulk structure of the nanofibers was analyzed using high-resolution transmission electron microscopy (HRTEM). A typical TEM image of the nanofibers is shown in Figure 1C,D. As Figure 1D reveals, the nanofibers are amorphous, with no indication of any crystalline impurities observed. Such an amorphous property is further confirmed by selected-area electron diffraction (SAED) analysis, as shown in Figure 1E as the presence of diffuse halos in the spectrum, a characteristic of amorphous structure. This is a type of allotropism, which is the first ever to be observed in Pt. Similar to the nanofibers, the quasi-spherical products also have amorphous structure (Figure 1F). This result infers that this structure could be the seed for nanofiber

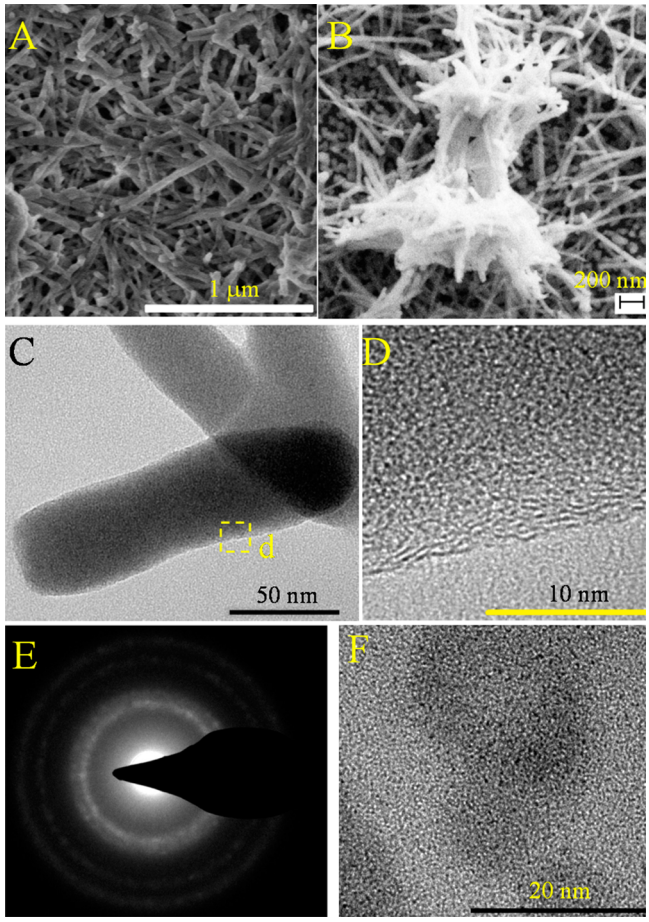

Figure 1. Typical FESEM (A and B) and TEM (C and D) images of a-Pt nanofibers. Part E shows the SAED spectrum of a-Pt. Part F is the TEM image of the nanoparticle byproducts.

growth on the substrate. Unfortunately, the a-Pt nanofibers are damaged and phase-transitioned under 200 kV electron-beam irradiation, forming single-crystalline, polycrystalline, and amorphous nanoparticles inside the structure. The crystalline Pt nanoparticles are mostly characterized by a high-energy lattice plane of (001) that is represented by the appearance of lattice-fringe spacing as long as 0.20 nm. Promising properties are expected to be generated from such amorphous fcc Pt nanostructure systems. The result is shown in Figure 2 (detailed phase transitions with time and phase transitions by product are shown in Figures S2 and S3 in the SI).

Considering that the fcc metal of Pt inherently forms a crystalline nanostructure because of its strong metallic bonding properties, the nanofibers could be organic solids that result from solidification of the surfactant molecules. We then performed EDX mapping to verify the element that composes the nanofibers and its distribution inside the structure. The result is shown in Figure 3. As Figure 3 reveals, the nanofibers are confirmed to be constructed by the Pt element instead of organic molecules (see Figure 3B). Elemental mapping also indicates that the Pt element is densely and homogeneously distributed over the nanofiber structure, even up to its outer surface. As observed from the analysis result, the Cl and N elements were detected in the nanofibers. Nevertheless, they are thought to come from the Pt precursor ($PtCl_6^{-2}$) and the surfactant for Cl and N, respectively, which attached to the nanofiber surface during the growth process. The image shows

DOI: 10.1021/acsami.5b01012
ACS Appl. Mater. Interfaces 2015, 7, 7776−7785

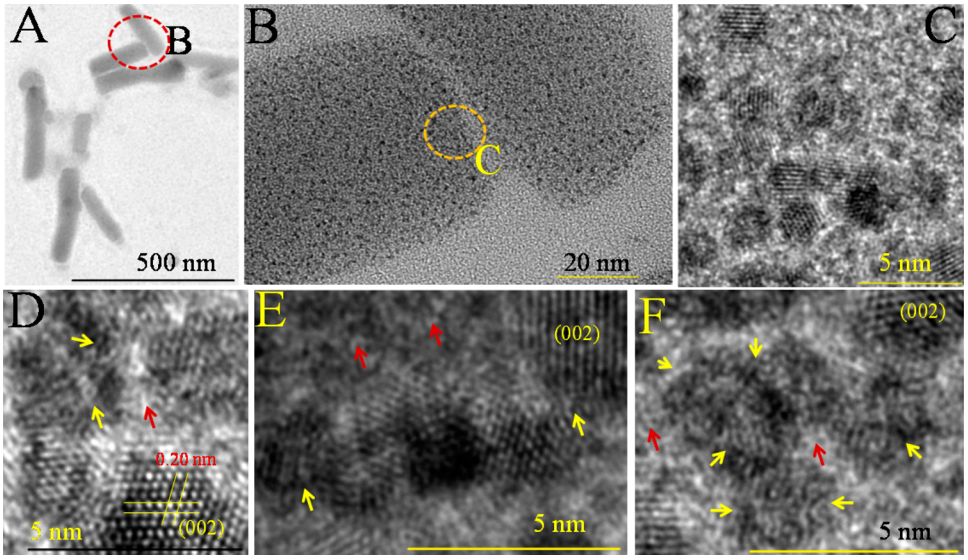

Figure 2. Phase transformation of the a-Pt nanofibers under electron-beam irradiation. (A) Typical low-resolution TEM image of nanofibers and (B and C) TEM images showing nanoparticle formation inside the nanofibers during analysis (for approximately 6 min). Typical nanoparticles formed during HRTEM analysis, i.e., single-crystalline (D), polycrystalline (E), and amorphous (F) nanoparticles. Yellow arrows indicate nanoparticles with amorphous structure, whereas red arrows indicate the amorphous structure at the region between two adjacent nanoparticles.

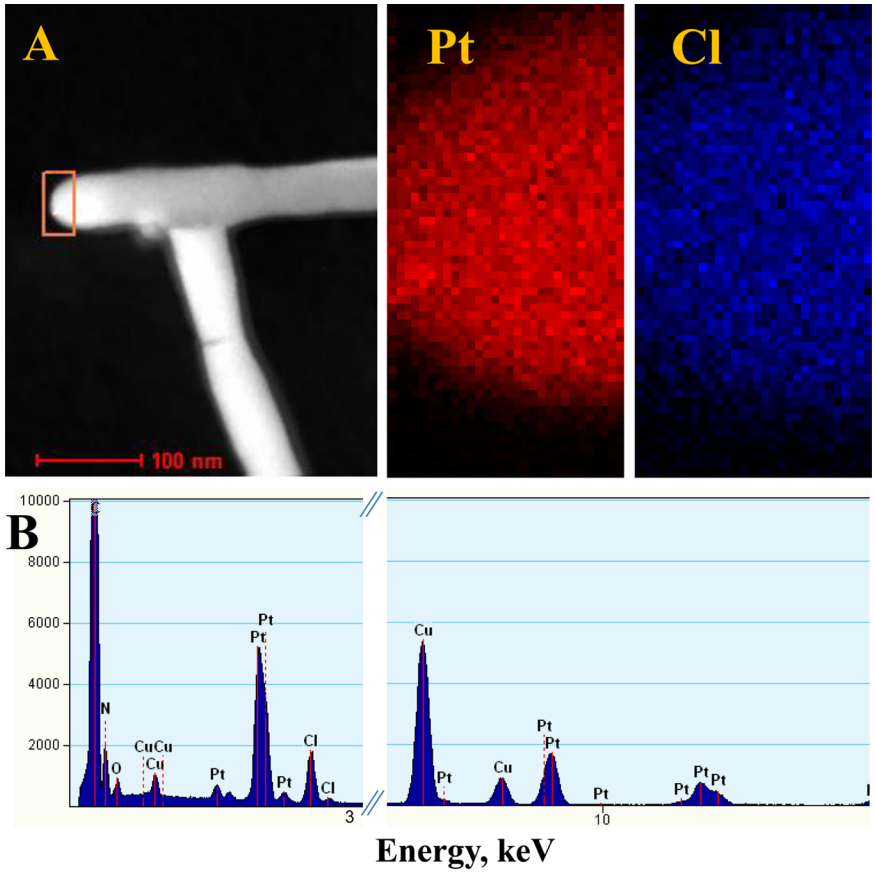

Figure 3. EDX mapping (A) and spectrum (B) of a-Pt nanofibers.

a typical atomic density profile for Cl, in which its density image is comparable to that of the Pt element in the nanofiber structure. However, atomic composition analysis reveals that its concentration is much lower compared to that of Pt (ca. 80%), namely, 10%. Actually, the same atomic density image was also obtained for N (not shown here), of which its atomic composition is also as high as 10%, as confirmed by the EDX spectrum shown in Figure 3B. We thought that such a dense distribution of these elements in elemental mapping is the result of their attachment on the surface of the nanofibers. Meanwhile, the Cu element was also observed from the spectrum, but it is simply from the TEM copper grid. On the

DOI: 10.1021/acsami.5b01012
ACS Appl. Mater. Interfaces 2015, 7, 7776−7785

basis of these results, it is confirmed that the structure is an a-Pt nanofiber.

We performed XPS analysis to elucidate the electronic structures and chemical state[31] of the a-Pt nanofibers. The results are shown in Figure 4. In agreement with the EDX

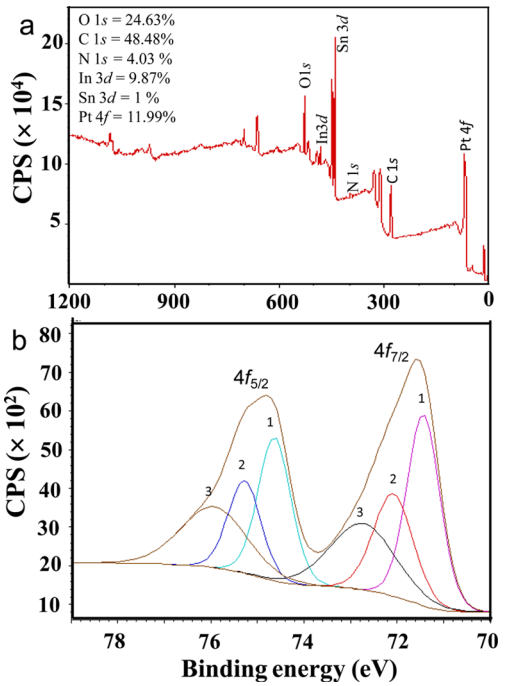

Figure 4. Broad-spectrum (A) and high-resolution (B) scans at the Pt binding energy of a-Pt nanofibers.

result, the Pt element was confirmed to be present in the spectrum along with the Sn, In, O, and N elements. It can be easily understood that the signal of Pt originated from the nanofibers and that the signals from Sn, In, and O are from the ITO substrate. Meanwhile, the signal N could be from the surfactant. A high-resolution scan after carbon correction was then performed at the Pt binding energy region to further identify the chemical state of the a-Pt nanofibers. Two pairs of Pt 4f curves were observed in the spectrum, which can be associated with the spin−orbital splitting of the 4f orbital, namely, $4f_{5/2}$ and $4f_{7/2}$ (see Figure 4B). Curve-fitting analysis on these spin−orbitals found that three GL curves fit each orbital. These results infer that at least two oxidation states of Pt are present in the nanofibers, namely, the Pt^0 (metallic) and Pt^{2+} oxidized states. For example, as shown in the $4f_{7/2}$ orbital in particular, the metallic state is present at the binding energy of 71.50 eV (curve 1) and two species of Pt^{2+} states (Pt coordination with different species will be discussed later) are present at the binding energies of 72.07 (curve 2) and 72.73 eV (curve 3).[32] As Figure 4B reveals, the metallic state is strong and dominant, confirming the metallic state of the a-Pt nanofibers. Nevertheless, the presence of the Pt^{2+} state in the spectrum, which has a reasonably high intensity, indicates that the a-Pt nanofiber surface is chemically reactive[33,34] and has the potential for catalysis and charge-transfer reactions. The high-oxidation chemical state should play an active role in the phase transition under electron-beam irradiation. In addition to these properties, the metallic state energy obtained in this analysis is positively shifted as high as 0.20 eV from the pure Pt (typically 71.30 eV), which indicates highly reactive surface properties[34] and the potential for catalysis applications.

The nonmetallic state intensity is relatively high in the XPS analysis result. One might say that the structure could be an impure a-Pt structure with foreign atoms or complexes of Pt contamination inside the structure. Although the detailed properties of the bulk structure of a-Pt were not obtained, particularly regarding the purity of the structure, the following facts confirm that the structure is a-Pt and not impure metallic state or Pt complexes. First, the intensity of the metallic state (Pt^0) is much higher than those of the nonmetallic states, a condition that is only possible in the amorphous or crystalline phase Pt. EDX elemental analysis, as shown in Figure 3, that demonstrates an extremely high atomic ratio of Pt (>90%) compared to Cl or other atoms further supports this assumption. With high-energy metallic bonding properties, the pure a-Pt nanostructure should be easily realized. Second, the presence of the Pt^{2+} states can be related to the complex formation on the surface of a-Pt with surfactant molecules [$Pt(NH_4)_2$, peak at 72.07 eV] and with OH^- species from the solvent [$Pt(OH)_2$, 72.73 eV]. The formation of Pt−PtO coordination on the nanofiber surface can also be considered for the spectrum at 72.73 eV, originating from ambient that formed during the sample preparation. Such a phenomenon is likely similar to the case of Pd−PdO bonding in the interface of a Pd−PdO core−shell nanocrystal, as reported in the literature.[35] Surface complex formation in this case is inevitable because it is required to stabilize the structure. This phenomenon was also observed earlier in the case of amorphous Pd nanoparticle formation.[27] Its high intensity is assumed merely because of the nature of the large number of surface atoms in the nanofiber structure that participate in the complex formation. FTIR analysis performed on the sample further confirms these assumption (see Figure 5). As Figure 5

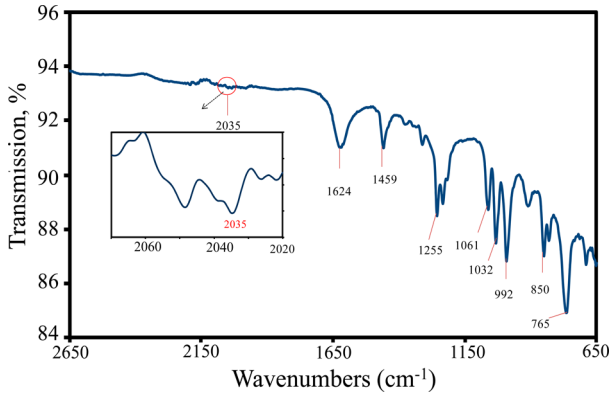

Figure 5. FTIR spectrum of a-Pt on the ITO substrate with Pt−Pt bond stretching (2035 cm^{-1}) and platinum amine vibration (1624 cm^{-1}). Bond vibration from the surfactant molecules is also observed, namely, C−H asymmetric bending (1459 cm^{-1}), C−N stretching (1255 cm^{-1}), C−O stretching (1061, 1032, and 992 cm^{-1}), and amine out-of-plane bending (850 and 765 cm^{-1}).

reveals, in addition to the presence of a Pt−Pt metallic state stretching vibration at 2035 cm^{-1} (lower by as much as 70 cm^{-1} compared to the Pt−Pt vibration energy in crystalline Pt system, the result of the less dense structure), the appearance of peaks at frequencies between 700 and 1800 cm^{-1} indicates a complexation process of surface atoms of a-Pt with the surfactant (i.e., platinum amine complex) that is most probable

DOI: 10.1021/acsami.5b01012
ACS Appl. Mater. Interfaces 2015, 7, 7776−7785

to occur on the surface of a-Pt only. In addition, judging from the EDX analysis result in Figure 3, Pt−Cl coordination is also expected in this case as another form of complexation of Pt nanofiber surface atoms,[36] which appears at the frequency below 500 cm^{-1}. Unfortunately, because of the limited capability of our apparatus, the spectrum below 650 cm^{-1} cannot be provided in this paper.

XPS analysis suggested that the a-Pt nanofibers have highly reactive surface properties resulting from the dominant metallic state with positive binding energy. These unique properties might find potential use in catalysis, and the performance in applications will be enhanced if the surface area is large. We performed BET analysis to obtain the available surface area on the substrate containing a-Pt nanofibers. In a typical procedure, following nitrogen gas adsorption and desorption at approximately −196 °C, a BET surface area as high as 146 $m^2\ g^{-1}$ was obtained from the a-Pt nanofibers on the substrate surface. This surface area is absolutely high in the viewpoint of nanostructures grown on a substrate surface. The sample is expected to provide a large-scale active site for chemical reaction. Because the nanofiber growth orientation on the surface is random, interconnection among the nanofibers creates a porous-like structure on the surface. BET analysis found that the adsorption and desorption pore diameters are approximately 61 and 47 nm, respectively, indicating that the fibrous structure creates a macroporous system on the surface. Thus, this condition is predicted to provide large-scale active sites for optimum surface reaction.

We hypothesize that a-Pt formation is the result of the synergetic role of both the reducing agent and surfactant molecules in influencing the nature of Pt crystallization and in modifying the high cohesive energy of the metallic bonding in the Pt nanocrystals. Nevertheless, how the reducing agent and surfactant modify the metallic bonding properties of Pt is not yet clear. We believe that formation of the amorphous structure is similar to the rapid cooling process in the formation of amorphous metal alloy systems.[18,19,26,37] A large amount of Pt ions should be reduced within a short period of time by formic acid for formation of the amorphous structure, increasing the chemical potential of the reaction and the entropy of the system, which cause solidification to end at a glassy state. HMT with its unique amine functional group[38] may form strong bonding with Pt atoms and play a complementary role in distorting the strong metallic bonding and highly symmetric properties of fcc Pt. A similar phenomenon was previously observed in the case of amorphous Pd nanoparticle formation.[27]

Formic acid is crucial for inducing anisotropic crystal growth in the Pt nanocrystals.[8] The use of different reducing agents with comparable reducing power, such as ascorbic acid or salicylic acid,[39] is incapable of promoting the one-dimensional structure of Pt[40] or other noble metals.[41,42] This could be due to the strong reducing power and dual functionalities, i.e., as an acid and as an aldehyde, which provide the possibility of rapidly reducing the metal ions and directing their nucleation. With an open-chain molecular structure, formic acid may have better control over one-dimensional crystal growth via effective adhesion onto the Pt lattice plane,[43] facilitated by its preferred bonding to the hydrogenized metal surface. HMT is assumed to act as an additional directing agent or soft template for one-dimensional nanocrystal growth.[3,44] HMT, with its active amine ligand in the molecular structure, is an efficient surfactant for surface passivation.[38] Its peculiar selective adhesion properties onto the nanostructure lattice plane make it able to promote one-dimensional nanocrystal growth in ZnO[45,46] as well as in noble metals, such as silver (Ag),[47] Pd,[48] and gold (Au).[49] It also promotes two-dimensional and platonic crystal growth in Au in combination with other surfactants.[50−52] In combination with the high-reducing power of formic acid, one-dimensional a-Pt nanofiber growth can be realized on the ITO substrate. Nevertheless, the nanofibers are projected from spherical nanoparticles, which were formed earlier on the substrate surface. With an increase of the reaction time and at a highly kinetic condition in the presence of HMT and a high concentration of formic acid, the spherical nanoparticles dissolve and grow (Oswald annealing process) into a nanofiber structure. These processes are evidenced in Figure 6. Earlier

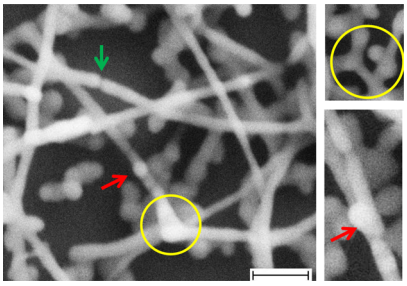

Figure 6. FESEM image showing the possible mechanism of nanofiber formation on the surface. The yellow circles highlight spherical nanoparticle dissolution to form one-dimensional crystal growth and branching. The red arrows show incomplete spherical nanoparticle dissolution into nanofibers. The green arrow indicates a collision between two elongated nanofibers. The scale bar is 100 nm.

growth analysis of the nanostructure further confirmed this process (see Figure S4 in the SI). For example, at 1 h of reaction time, the Pt nanostructure formed on the surface was only high-density spherical particles of sizes in the range of 30−50 nm. When the growth time was extended to 2 h, nanoneedle structures began to form on the substrate. However, the yield was relatively low. High-density nanofibers of a-Pt were obtained when the growth time was increased to 4 h.

The formation a-Pt nanofibers on the ITO substrate is sensitive to the reaction conditions, in particular, the reaction temperature and concentration of formic acid and HMT used in the reaction. A temperature of 40 °C was the optimum for high-density nanofiber growth. Lower temperature may lead to the formation of spherical nanostructures only, whereas higher temperature produced a spherical nanoparticle network arranged in a threadlike shape; their yield is relatively low and is not homogeneously distributed over the substrate surface. The FESEM image of the Pt nanostructures prepared at different growth temperatures is shown in Figure S5 in the SI. For formic acid, the concentration that promotes the formation of high-density a-Pt nanofibers is at least 0.5 M, but the optimum is 1.0 M. If a lower concentration is used, nanofibers with low density are produced. This could be due to the limited power of formic acid to trigger the formation of a nanofiber structure, which is enhanced at higher concentrations. Vice versa, if a higher concentration is used, nanofibers with truncated morphology and a high degree of surface defects and inhomogeneity in their diameter and length are obtained, indicating the occurrence of active deformation in the nanostructure due to the excessive reducing power in the reaction. The results are shown in Figure S6 in the SI. Finally,

DOI: 10.1021/acsami.5b01012
ACS Appl. Mater. Interfaces 2015, 7, 7776−7785

for HMT, a low concentration, namely, in the range of 0.01−0.015 M, is sufficient to induce the formation of high-density a-Pt nanofibers. If a higher concentration were used, for example, 0.02 M, low-density nanofibers of longer length were obtained. At an extremely high concentration, long nanofibers with an excess amount of HMT layer attachment on the surface were obtained. However, no nanofiber formation was obtained if there was no HMT in the reaction. The results are shown in Figure S7 in the SI.

3.2. Heterogeneous Catalytic Characterization. The heterogeneous catalytic properties of the synthesized a-Pt nanofibers were evaluated in the hydrogenation of acetone to produce isopropyl alcohol under microwave irradiation. In the typical procedure, 10.0 mL of 0.1 mol L^{-1} aqueous acetone was subjected to microwave irradiation, and the hydrogenation of acetone was examined by recording the change in the optical absorption of acetone, particularly at its characteristic absorption band centered at 265 nm, every 10 s during the reaction. Prior to evaluating the catalytic hydrogenation of acetone by a-Pt nanofibers, we examined the effect of the microwave irradiation power in the absence of an a-Pt nanofiber catalyst on the acetone hydrogenation to determine the extent of microwave power required for the hydrogenation process. Figure 7 shows typical UV−visible spectra and

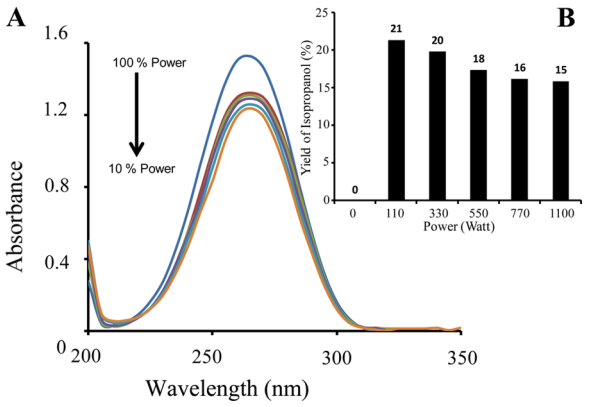

Figure 7. Effect of the microwave irradiation power on acetone hydrogenation to isopropyl alcohol. (A) Acetone optical absorption spectra under different microwave irradiation power and (B) its corresponding isopropyl alcohol yield.

absorbance changes of the center absorption band of acetone under varying microwave irradiation power, from 110 to 1100 W, within 1 min of reaction time. From Figure 7A, it can be observed that the absorbance decreases when the power of the microwave is reduced from 1100 W. The maximum decrease was observed at the lowest microwave power, i.e., 110 W. From the absorption profile, we know that isopropyl alcohol is formed during the reaction, and its yield, based on Figure S1 in the SI, decreased from 21 to 15% with increasing microwave irradiation power. The decrease in the yield of isopropyl alcohol upon increasing the microwave irradiation power is due to the result of the temperature increase in the reaction, which favors the formation of isobutyl ketone instead of isopropyl alcohol.[53] The histogram for the isopropyl alcohol yield versus the applied microwave irradiation power is shown in Figure 7B. In this study, we did not use a chemical as a source of hydrogen, for example, $NaBH^{-}_{4}$, as reported in our previous paper.[28] Water itself is often used as a hydrogen source, as reported by Tomin et al., to perform the hydrogenation of acetone to isopropyl alcohol.[54] As we mentioned in the Experimental Section, because the glass vial containing the acetone solution was placed in a Teflon-sealed tube, which increases the pressure during the reaction, water molecules may split and provide hydrogen to perform the hydrogenation of acetone. Because the microwave power of 110 W gave the highest yield of isopropyl alcohol, we used this power for further studies.

Subsequently, the kinetics of the hydrogenation of acetone were determined in the presence of an a-Pt nanofiber catalyst. In this study, one ITO slide containing an a-Pt nanofiber catalyst was used. Figure 8 shows the kinetic heterogeneous

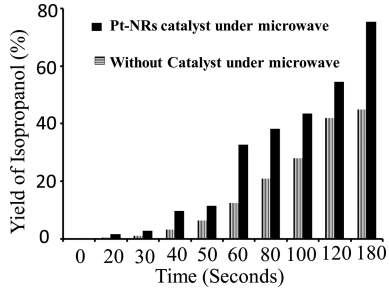

Figure 8. Acetone hydrogenation with and without the presence of an a-Pt nanofiber catalyst.

catalytic hydrogenation of acetone by a-Pt nanofibers under 110 W microwave irradiation monitored from 10 to 180 s. Figure 8 reveals that the yield of isopropyl alcohol significantly increased with increasing reaction time. At 180 s, the isopropyl alcohol produced in the presence of an a-Pt nanofiber catalyst can reach approximately 75% (solid black bar), almost double compared to the yield without the presence of a nanocatalyst (gray bar). This conversion value might be insignificant if observed from the yield of acetone hydrogenation without and with catalyst under microwave irradiation. Nevertheless, if considered from the point of view of the catalyst mass on the ITO surface, typically 30 μg, which is vulnerable to catalyst surface deactivation and poisoning, the acetone hydrogenation yield in the presence of catalyst is considerably high. The yield can be further improved when the amount of the ITO slide containing a-Pt catalyst is increased.

Up to this stage, the success of the hydrogenation reaction was judged solely on the basis of optical absorption spectroscopy. To further verify that the hydrogenation reaction of acetone was successful, we performed HPLC analysis of the aqueous acetone solution after 180 s under hydrogenation reaction. The result is shown in Figure S8 in the SI. As observed from the result, two well-separated peaks are present in the chromatogram, which are directly attributed to acetone and isopropyl alcohol, with retention times of 25.67 and 28.13 min, respectively. On the basis of this result, the hydrogenation reaction of acetone to isopropyl alcohol was successful under the present reaction process.

To obtain the TON and TOF values of the a-Pt nanofiber catalyst, we approximated the active site on the catalyst using the surface area of the a-Pt nanofiber on the substrate surface, as calculated via BET analysis (see the SI for the detailed BET analysis experiment and results). In a typical result, a surface area as high as 117 m^2 g^{-1}, equivalent to a specific surface area of 0.0035 m^2, for a single ITO slide containing a-Pt nanofibers (mass 30 μg) was obtained. Because the dynamic cross section of a single acetone molecule is approximately 1.66×10^{-19} m^2

DOI: 10.1021/acsami.5b01012
ACS Appl. Mater. Interfaces 2015, 7, 7776−7785

(diameter ~ 4.6×10^{-10} m^2), the available active sites on the catalyst surface for a single ITO slide are as high as 2×10^{16} sites. The TON and TOF values of acetone hydrogenation at 180 s of reaction time reach 213 and 71 min^{-1}, respectively. As is normal in the surface reaction process in which only the most accessible sites take part in the reaction, the TON and TOF values can be much higher. By considering the nature of the a-Pt nanofiber structure and morphology, 20−30% of the available surface may play a role in the reaction. Thus, the TON and TOF values could be doubled to 400 and 140 min^{-1}, respectively. These values are astoundingly high in the case of heterogeneous catalytic reaction compared to recently reported results[55] (see Table 1), confirming the high efficiency of the a-Pt nanofiber catalyst.

Table 1. Comparison of the Catalytic Efficiency of the a-Pt Nanofiber Catalyst for Acetone Hydrogenation with Other Catalysts

no.	catalyst	catalyst mass	reaction time	% of degradation	ref
1	a-Pt nanofiber[a]	30 μg	2 min	40	present study
2	Pd hollow nanoparticles[b]	0.7 μg	5 min	66.4	28
3	Raney Ni[c]	29 g	1.5 h	99.8	55
4	PtGa[d]	50 mg	12 h	88	56
5	Rh[d]	200 mg	13 h	98	56

[a]Microwave irradiation (110 W) was applied. [b]$NaBH_4$ (0.1 mM) was used as the hydrogen source. [c]Temperature of 80 °C and hydrogen applied. [d]Temperature of higher than 100 °C and hydrogen used.

The TON and TOF calculations used the total acetone hydrogenation in the presence of catalyst without considering the contribution of the microwave effect on the reaction because the nature of the hydrogenation reaction will be completely different in the presence and absence of catalyst. For example, the hydrogenation reaction might be much more active on the catalyst compared to the effect of microwave irradiation. Therefore, the effect of microwave irradiation in the reaction cannot be simply subtracted from the yield in the calculation of TON and TOF of the a-Pt catalyst. The use of different methods, such as the addition of $NaBH_4$ as the source of hydrogen in the reaction, instead of microwave irradiation, could further probe the detailed catalytic properties of a-Pt.

The high catalytic efficiency of the a-Pt nanofibers can be attributed to (i) the nature of the nanofiber structure with a disordered atomic arrangement and peculiar surface chemistry properties and (ii) the wide surface area of the active site on the nanofiber structure. One point to be noted here is that the isopropyl alcohol generation slowed with increased reaction time. Similar to the case of high-power microwave irradiation mentioned earlier, the decrease in the isopropyl alcohol yield with increased reaction time is due to an increase in the reaction temperature, which promotes the formation of isobutyl ketone instead of isopropyl alcohol.[53]

In the hydrogenation reaction, the Langmuir−Hinshelwood mechanism is valid, in which the hydrogen that is produced in the reaction is absorbed by the catalyst surface and attacks the C═C double bond in acetone (which is also absorbed on the catalyst surface), producing isopropyl alcohol.[28,57] Isopropyl alcohol immediately desorbs after its formation.

To investigate the parameters that influence the heterogeneous catalytic reaction of acetone on the a-Pt nanofibers, the Langmuir−Hinshelwood pseudo-first-order and pseudo-second-order kinetic models were used to analyze the experimental kinetic data.[57] The reaction follows the pseudo-first-order kinetics with a fitting coefficient of $R^2 > 0.99$. The pseudo-first-order rate coefficient is as high as 8.0×10^{-3} min^{-1}, indicating a reasonably high reaction rate. The high values of the R^2 coefficients of the pseudo-first-order model illustrate that the reaction, which occurs at a specific rate, depends linearly on the concentration of acetone in the catalysis process. Figure 9 shows a typical Langmuir−Hinshelwood pseudo-first-order kinetic hydrogenation of acetone onto the a-Pt nanofiber catalyst. The absence of the effect of other parameters, such as the solvent, catalyst structure, and morphology effects, which can be described using higher-order pseudokinetic models, is due to the highly active a-Pt nanofiber catalyst.

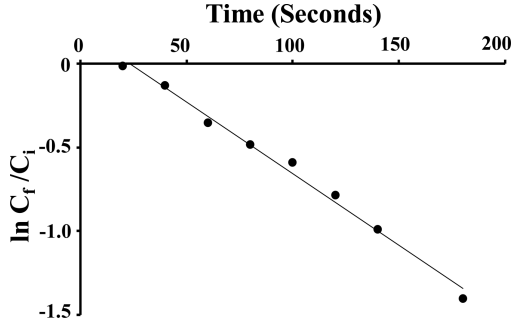

Figure 9. Typical Langmuir−Hinshelwood pseudo-first-order kinetic hydrogenation of acetone.

Because the catalytic capability depends on the moles of catalyst involved in the reaction, we expected higher catalytic capability if the number of ITO slides containing a-Pt nanofiber catalyst involved in the reaction were increased. Thus, we used two ITO slides containing a-Pt nanofibers in the reaction. This was also meant to validate the effectiveness of the proposed method to produce a highly active a-Pt nanofiber catalyst for heterogeneous catalysis applications. When the microwave power, acetone concentration, and experimental procedure were kept unchanged, the heterogeneous catalytic hydrogenation of the acetone performance of the sample was evaluated. A drastic change in the optical absorption of acetone, which was approximately 4 times higher compared to using a single ITO slide, was observed upon a brief (20 s) introduction of the two ITO slides containing a-Pt nanofibers. This process rapidly evolved with time, and the reaction was completed as quickly as 120 min, producing approximately 100% yield of isopropyl alcohol, which is 2 times faster compared to using one ITO slide containing a-Pt nanofibers (75% yield within 180 s). The result is shown in Figure 10. The nanocatalyst properties and capability are fixed even when grown on a different ITO substrate, confirming the reproducibility of the method to produce highly efficient a-Pt nanofiber catalysts on the ITO surface.

The catalytic properties of the a-Pt nanofibers presented here are remarkably high in terms of heterogeneous reaction. Because the catalytic reaction depends on several parameters, in particular the surface chemistry of the nanocatalyst, further analysis on this point, such as using temperature-programmed reduction and desorption for hydrogen analysis, is necessary to support the UV−visible absorption spectroscopy result. This

DOI: 10.1021/acsami.5b01012
ACS Appl. Mater. Interfaces 2015, 7, 7776−7785

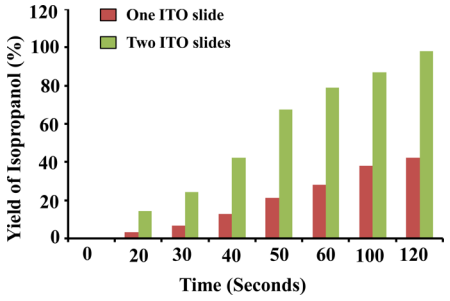

Figure 10. Effect of the amount of catalyst on acetone hydrogenation.

analysis is being performed, and the result will be reported in a forthcoming paper.

4. CONCLUSIONS

An efficient strategy to grow large-scale, a-Pt nanofibers directly on an ITO substrate surface using a mild, one-pot synthesis method in aqueous solution containing a Pt precursor, a HMT surfactant, and a formic acid strong reducing agent has been demonstrated. The combined effect of the strong reduction power of formic acid and HMT surfactant is the key factor for modification of the metallic bonding characteristics of fcc Pt for amorphous structure formation. The XPS analysis result indicated that a-Pt is metallic, with highly reactive surface properties resulting from the dominant metallic state of Pt with a positive energy shift and the Pt^{2+} state. The new structure of Pt exhibits excellent catalytic properties in the acetone hydrogenation reaction to produce isopropyl alcohol with TON and TOF as high as 400 and 140 min^{-1}, respectively. Thus, the catalyst promises enhanced performance in catalysis, sensors, and electrochemistry applications. Because of the unique disordered atomic arrangement, more novel properties are expected to be produced from the a-Pt nanostructure for enhanced performance in currently existing applications.

■ ASSOCIATED CONTENT

Supporting Information

Phase transition under electron-beam irradiation, FESEM of a-Pt prepared using different growth temperatures, formic acid and HMT concentrations, and HPLC analysis as well as BET analysis and TON and TOF calculation. This material is available free of charge via the Internet at http://pubs.acs.org.

■ AUTHOR INFORMATION

Corresponding Author

*E-mail: akrajas@ukm.edu.my. Tel.: +603 8911 8547. Fax: +603 8925 0439.

Notes

The authors declare no competing financial interest.

■ ACKNOWLEDGMENTS

The authors are grateful for financial support received from the Ministry of Higher Education of Malaysia under the research fundamental FRGS/2/2013/SG02/UKM/02/8 and the HiCOE project (AKU 95) and the Universiti Kebangsaan Malaysia under the DIP-2012-16 project.

■ REFERENCES

(1) Bratlie, K. M.; Lee, H.; Komvopoulos, K.; Yang, P.; Somorjai, G. A. Platinum Nanoparticle Shape Effects on Benzene Hydrogenation Selectivity. *Nano Lett.* **2007**, *7*, 3097−3101.

(2) Subhramannia, M.; Pillai, V. K. Shape-dependent electrocatalytic activity of platinum nanostructures. *J. Mater. Chem.* **2008**, *18*, 5858−5870.

(3) Krishnaswamy, R.; Remita, H.; Impéror-Clerc, M.; Even, C.; Davidson, P.; Pansu, B. Synthesis of Single-Crystalline Platinum Nanorods within a Soft Crystalline Surfactant−Pt^{II} Complex. *ChemPhysChem* **2006**, *7*, 1510−1513.

(4) Lewis, L. N.; Lewis, N. Platinum-catalyzed hydrosilylation—colloid formation as the essential step. *J. Am. Chem. Soc.* **1986**, *108*, 7228−7231.

(5) He, S.; Sun, C.; Bai, Z.; Dai, X.; Wang, B. Dehydrogenation of long chain paraffins over supported Pt−Sn−K/Al_2O_3 catalysts: A study of the alumina support effect. *Appl. Catal., A* **2009**, *356*, 88−98.

(6) Narayanan, R. Recent Advances in Noble Metal Nanocatalysts for Suzuki and Heck Cross-Coupling Reactions. *Molecules* **2010**, *15*, 2124−2138.

(7) Colacot, T. J.; Qian, H.; Cea-Olivares, R.; Hernandez-Ortega, S. Synthesis, X-ray, spectroscopic and a preliminary Suzuki coupling screening studies of a complete series of dppfMX_2 (M = Pt, Pd; X = Cl, Br, I). *J. Organomet. Chem.* **2001**, *637−639*, 691−697.

(8) Balouch, A.; Umar, A. A.; Tan, S. T.; Nafisah, S.; Md Saad, S. K.; Salleh, M. M.; Oyama, M. Fibrous, ultra-small nanorod-constructed platinum nanocubes directly grown on the ITO substrate and their heterogeneous catalysis application. *RSC Adv.* **2013**, *3*, 19789−19792.

(9) Liang, C. C.; Juliard, A. L. Reduction of Oxygen at the Platinum Electrode. *Nature* **1965**, *207*, 629−630.

(10) Gratzel, M. Photoelectrochemical cells. *Nature* **2001**, *414*, 338−344.

(11) O'Regan, B.; Gratzel, M. A low-cost, high-efficiency solar cell based on dye-sensitized colloidal TiO_2 films. *Nature* **1991**, *353*, 737−740.

(12) Carpenter, M. K.; Moylan, T. E.; Kukreja, R. S.; Atwan, M. H.; Tessema, M. M. Solvothermal Synthesis of Platinum Alloy Nanoparticles for Oxygen Reduction Electrocatalysis. *J. Am. Chem. Soc.* **2012**, *134*, 8535−8542.

(13) Guo, S.; Wen, D.; Zhai, Y.; Dong, S.; Wang, E. Platinum Nanoparticle Ensemble-on-Graphene Hybrid Nanosheet: One-Pot, Rapid Synthesis, and Used as New Electrode Material for Electrochemical Sensing. *ACS Nano* **2010**, *4*, 3959−3968.

(14) Surendran, G.; Apostolescu, G.; Tokumoto, M.; Prouzet, E.; Ramos, L.; Beaunier, P.; Kooyman, P. J.; Etcheberry, A.; Remita, H. From Self-Assembly of Platinum Nanoparticles to Nanostructured Materials. *Small* **2005**, *1*, 964−967.

(15) Demetriou, M. D.; Launey, M. E.; Garrett, G.; Schramm, J. P.; Hofmann, D. C.; Johnson, W. L.; Ritchie, R. O. A damage-tolerant glass. *Nat. Mater.* **2011**, *10*, 123−128.

(16) Hofmann, D. C.; Suh, J.-Y.; Wiest, A.; Duan, G.; Lind, M.-L.; Demetriou, M. D.; Johnson, W. L. Designing metallic glass matrix composites with high toughness and tensile ductility. *Nature* **2008**, *451*, 1085−1089.

(17) Hauser, J. J. Electrical and Structural Properties of Amorphous Metal\char22{}Metal-Oxide Systems. *Phys. Rev. B* **1973**, *7*, 4099−4111.

(18) Bhat, M. H.; Molinero, V.; Soignard, E.; Solomon, V. C.; Sastry, S.; Yarger, J. L.; Angell, C. A. Vitrification of a monatomic metallic liquid. *Nature* **2007**, *448*, 787−790.

(19) Klement, W.; Willens, R. H.; Duwez, P. O. L. Non-crystalline Structure in Solidified Gold−Silicon Alloys. *Nature* **1960**, *187*, 869−870.

(20) Liebermann, H. H.; Graham, C. D. Production of amorphous alloy ribbons and effects of apparatus parameters on ribbon dimensions. *IEEE Trans. Magn.* **1976**, *12*, 921−923.

(21) Das, J.; Tang, M. B.; Kim, K. B.; Theissmann, R.; Baier, F.; Wang, W. H.; Eckert, J. "Work-Hardenable" Ductile Bulk Metallic Glass. *Phys. Rev. Lett.* **2005**, *94*, 205501.

(22) Zhang, B.; Zhao, D. Q.; Pan, M. X.; Wang, W. H.; Greer, A. L. Amorphous Metallic Plastic. *Phys. Rev. Lett.* **2005**, *94*, 205502.

DOI: 10.1021/acsami.5b01012
ACS Appl. Mater. Interfaces 2015, 7, 7776−7785

(23) Ding, S.; Liu, Y.; Li, Y.; Liu, Z.; Sohn, S.; Walker, F. J.; Schroers, J. Combinatorial development of bulk metallic glasses. *Nat. Mater.* **2014**, *13*, 494−500.
(24) Suslick, K. S.; Choe, S.-B.; Cichowlas, A. A.; Grinstaff, M. W. Sonochemical synthesis of amorphous iron. *Nature* **1991**, *353*, 414−416.
(25) Zhong, L.; Wang, J.; Sheng, H.; Zhang, Z.; Mao, S. X. Formation of monatomic metallic glasses through ultrafast liquid quenching. *Nature* **2014**, *512*, 177−180.
(26) Davies, H. A.; Aucote, J.; Hull, J. B. Amorphous nickel produced by splat quenching. *Nature* **1973**, *246*, 13−14.
(27) Hu, G.; Sharifi, T.; Nitze, F.; Barzegar, H. R.; Tai, C.-W.; Wågberg, T. Phase-transfer synthesis of amorphous palladium nanoparticle-functionalized 3D helical carbon nanofibers and its highly catalytic performance towards hydrazine oxidation. *Chem. Phys. Lett.* **2012**, *543*, 96−100.
(28) Balouch, A.; Ali Umar, A.; Shah, A. A.; Mat Salleh, M.; Oyama, M. Efficient heterogeneous catalytic hydrogenation of acetone to isopropanol on semihollow and porous palladium nanocatalyst. *ACS Appl. Mater. Interfaces* **2013**, *5*, 9843−9849.
(29) Umar, A. A.; Rahmi, E.; Balouch, A.; Abd Rahman, M. Y.; Salleh, M. M.; Oyama, M. Highly-reactive AgPt nanofern composed of {001}-faceted nanopyramidal spikes for enhanced heterogeneous photocatalysis application. *J. Mater. Chem. A* **2014**, *2*, 17655−17665.
(30) Tan, S. T.; Umar, A. A.; Balouch, A.; Yahaya, M.; Yap, C. C.; Salleh, M. M.; Oyama, M. ZnO nanocubes with (1 0 1) basal plane photocatalyst prepared via a low-frequency ultrasonic assisted hydrolysis process. *Ultrason. Sonochem.* **2014**, *21*, 754−760.
(31) Chiu, C.-Y.; Chung, P.-J.; Lao, K.-U.; Liao, C.-W.; Huang, M. H. Facet-Dependent Catalytic Activity of Gold Nanocubes, Octahedra, and Rhombic Dodecahedra toward 4-Nitroaniline Reduction. *J. Phys. Chem. C* **2012**, *116*, 23757−23763.
(32) He, D.; Cheng, K.; Peng, T.; Sun, X.; Pan, M.; Mu, S. Bifunctional effect of reduced graphene oxides to support active metal nanoparticles for oxygen reduction reaction and stability. *J. Mater. Chem.* **2012**, *22*, 21298−21304.
(33) Yoon, J.; Khi, N. T.; Kim, H.; Kim, B.; Baik, H.; Back, S.; Lee, S.; Lee, S.-W.; Kwon, S. J.; Lee, K. High yield synthesis of catalytically active five-fold twinned Pt nanorods from a surfactant-ligated precursor. *Chem. Commun.* **2013**, *49*, 573−575.
(34) Şen, F.; Gökağaç, G. Different Sized Platinum Nanoparticles Supported on Carbon: An XPS Study on These Methanol Oxidation Catalysts. *J. Phys. Chem. C* **2007**, *111*, 5715−5720.
(35) Gracia-Espino, E.; Hu, G.; Shchukarev, A.; Wågberg, T. Understanding the Interface of Six-Shell Cuboctahedral and Icosahedral Palladium Clusters on Reduced Graphene Oxide: Experimental and Theoretical Study. *J. Am. Chem. Soc.* **2014**, *136*, 6626−6633.
(36) Allen, A. D.; Theophanides, T. Platinum(II) Complexes: Infrared Spectra in the 300−800 cm−1 Region. *Can. J. Chem.* **1964**, *42*, 1551−1554.
(37) Greer, A. L. Metallic Glasses. *Science* **1995**, *267*, 1947−1953.
(38) Barone, G.; Crescenzi, V.; Liquori, A. M.; Quadrifoglio, F. Physicochemical properties of hexamethylenetetramine aqueous solutions. *J. Phys. Chem.* **1967**, *71*, 984−986.
(39) Benaissi, K.; Johnson, L.; Walsh, D. A.; Thielemans, W. Synthesis of platinum nanoparticles using cellulosic reducing agents. *Green Chem.* **2010**, *12*, 220−222.
(40) Chang, G.; Oyama, M.; Hirao, K. In Situ Chemical Reductive Growth of Platinum Nanoparticles on Indium Tin Oxide Surfaces and Their Electrochemical Applications. *J. Phys. Chem. B* **2006**, *110*, 1860−1865.
(41) Murphy, C. J.; Gole, A. M.; Hunyadi, S. E.; Orendorff, C. J. One-Dimensional Colloidal Gold and Silver Nanostructures. *Inorg. Chem.* **2006**, *45*, 7544−7554.
(42) Murphy, C. J.; Sau, T. K.; Gole, A. M.; Orendorff, C. J.; Gao, J.; Gou, L.; Hunyadi, S. E.; Li, T. Anisotropic Metal Nanoparticles: Synthesis, Assembly, and Optical Applications. *J. Phys. Chem. B* **2005**, *109*, 13857−13870.
(43) Peterson, M. R.; Csizmadia, I. G. Determination and analysis of the formic acid conformational hypersurface. *J. Am. Chem. Soc.* **1979**, *101*, 1076−1079.
(44) Liu, B.-H.; Yu, S.-H.; Chen, S.-F.; Wu, C.-Y. Hexamethylenetetramine Directed Synthesis and Properties of a New Family of α-Nickel Hydroxide Organic−Inorganic Hybrid Materials with High Chemical Stability. *J. Phys. Chem. B* **2006**, *110*, 4039−4046.
(45) Vayssieres, L. Growth of arrayed nanorods and nanowires of ZnO from aqueous solutions. *Adv. Mater.* **2003**, *15*, 464−466.
(46) Gao, X.; Li, X.; Yu, W. Flowerlike ZnO Nanostructures via Hexamethylenetetramine-Assisted Thermolysis of Zinc−Ethylenediamine Complex. *J. Phys. Chem. B* **2005**, *109*, 1155−1161.
(47) Umar, A. A.; Oyama, M.; Salleh, M. M.; Majlis, B. Y. Silver nanocombs and branched nanowires formation in aqueous binary surfactants solution. *J. Nanopart. Res.* **2012**, *14*, 1−9.
(48) Umar, A. A.; Oyama, M. Synthesis of palladium nanobricks with atomic-step defects. *Cryst. Growth Des.* **2008**, *8*, 1808−1811.
(49) Umar, A. A.; Oyama, M. High-yield synthesis of tetrahedral-like gold nanotripods using an aqueous binary mixture of cetyltrimethylammonium bromide and hexamethylenetetramine. *Cryst. Growth Des.* **2009**, *9*, 1146−1152.
(50) Ali Umar, A.; Oyama, M.; Mat Salleh, M.; Yeop Majlis, B. Formation of highly thin, electron-transparent gold nanoplates from nanoseeds in ternary mixtures of cetyltrimethylammonium bromide, poly(vinyl pyrrolidone), and poly(ethylene glycol). *Cryst. Growth Des.* **2010**, *10*, 3694−3698.
(51) Umar, A. A.; Oyama, M.; Salleh, M. M.; Majlis, B. Y. Formation of high-yield gold nanoplates on the surface: Effective two-dimensional crystal growth of nanoseed in the presence of poly(vinylpyrrolidone) and cetyltrimethylammonium bromide. *Cryst. Growth Des.* **2009**, *9*, 2835−2840.
(52) Umar, A. A.; Salleh, M. M.; Majlis, B. Y.; Oyama, M. Formation of high-density crystalline-shape gold nanoparticles on indium tin oxide surfaces: Effects of alcohothermal seeding. *J. Nanosci. Nanotechnol.* **2011**, *11*, 4974−4980.
(53) Narayanan, S.; Unnikrishnan, R. Acetone hydrogenation over co-precipitated Ni/Al_2O_3, Co/Al_2O_3 and Fe/Al_2O_3 catalysts. *J. Chem. Soc., Faraday Trans.* **1998**, *94*, 1123−1128.
(54) Tomin, A.; Lazarev, A.; Bere, M. P.; Redjeb, H.; Török, B. Selective reduction of ketones using water as a hydrogen source under high hydrostatic pressure. *Org. Biomol. Chem.* **2012**, *10*, 7321−7326.
(55) Chang, N.-S.; Aldrett, S.; Holtzapple, M. T.; Davison, R. R. Kinetic studies of ketone hydrogenation over Raney nickel catalyst. *Chem. Eng. Sci.* **2000**, *55*, 5721−5732.
(56) van Druten, G. M. R.; Ponec, V. Hydrogenation of carbonylic compounds: Part I: Competitive hydrogenation of propanal and acetone over noble metal catalysts. *Appl. Catal., A* **2000**, *191*, 153−162.
(57) Tripolskii, A. I.; Pavlenko, N. V.; Talbiz, G. M.; Golodets, G. I. Kinetics and mechanism of acetone hydrogenation on nickel and palladium catalysts. *React. Kinet. Catal. Lett.* **1983**, *22*, 367−370.

DOI: 10.1021/acsami.5b01012
ACS Appl. Mater. Interfaces 2015, 7, 7776−7785